Gilbert damping of NiFe thin films grown on two-dimensional chiral hybrid lead-iodide perovskites

Tempei Hatajiri,[1] Shoya Sakamoto,[1,*] Hidetoshi Kosaki,[1] Zikang Tian,[1] Miuko Tanaka,[1] Toshiya Ideue,[1] Keiichi Inoue,[1] Daigo Miyajima,[2,3] and Shinji Miwa[1,4,†]

[1]*The Institute for Solid State Physics, The University of Tokyo, Chiba 277-8581, Japan*

[2]*Center for Emergent Matter Science (CEMS), RIKEN, Wako, Saitama 351-0198, Japan*

[3]*School of Science and Engineering, The Chinese University of Hong Kong, Shenzhen, Guangdong 518172, China*

[4]*Trans-scale Quantum Science Institute, The University of Tokyo, Bunkyo, Tokyo 113-0033, Japan*

(Received 3 March 2024; revised 5 July 2024; accepted 31 July 2024; published 23 August 2024)

The phenomenon of chirality-induced spin selectivity (CISS) refers to the coupling between structural chirality and the spin polarization of conduction electrons. While previous studies of CISS have primarily focused on systems exhibiting charge current flow, our investigation aims to explore CISS within a charge-current-free environment. This approach is intended to overcome the challenges posed by pinholes in chiral molecular films. In this study, we investigated the Gilbert damping of NiFe layers deposited on two-dimensional chiral hybrid lead-iodide perovskites, utilizing the time-resolved magneto-optical Kerr effect. Our results reveal a minor variation in the Gilbert damping constant on the magnetization direction of the NiFe. This subtle change in the damping constant, observed when pure spin current is injected from NiFe to the chiral perovskite via spin pumping, aligns with previous observations of modest CISS-induced magnetoresistance in a multilayer device, contrasting with the significant magnetoresistance detected in spin-polarized conductive atomic force microscopy measurements. Our findings contribute valuable insight into the understandings of CISS-related phenomena, paving the way for further research in this field.

DOI: 10.1103/PhysRevB.110.054435

I. INTRODUCTION

Spin polarization in chiral molecules, extensively explored under the framework of chirality-induced spin selectivity (CISS), has attracted significant attention in recent research [1–7]. The phenomenon is generally attributed to the interplay between structural chirality, electric current, and spin-orbit interaction, leading to current-induced spin polarization. However, recent studies suggest the occurrence of spin polarization without the need for a bias electric current [8–13], indicating that a comprehensive understanding of CISS remains elusive. Predominantly, CISS investigations have utilized a system incorporating electric current, typically through a two-terminal device that combines a chiral molecule with a ferromagnetic metal. Despite theoretical skepticism regarding the feasibility of the CISS-induced magnetoresistance (MR) effect in such configurations [14], experimental evidence confirms their presence at room temperature [2,4–7]. A notably perplexing issue is the observed substantial variance in MR ratios between spin-polarized conductive atomic force microscopy measurements and multilayer device assessments, despite using identical material systems. This discrepancy might be linked to pinholes within multilayer film devices, though the specifics remain unresolved [5,6]. In this paper, our objective is to delve into CISS-related phenomena absent of electric current injection into chiral molecules. By omitting the bias electric current, we sidestep the complications associated with pinholes in chiral molecule films. Our approach involves a bilayer system composed of two-dimensional (2D) chiral hybrid lead-iodide perovskite [5] [Fig. 1(a)] and NiFe, where spin pumping [15–17] facilitates the pure spin current injection into chiral molecules. The process is analyzed by evaluating the Gilbert damping constant of NiFe using the time-resolved magneto-optical Kerr effect (TRMOKE).

II. EXPERIMENT

2D chiral hybrid lead-iodide perovskites, (*R*)-(+)-α-methylbenzylammonium lead iodide and (*S*)-(−)-α-methylbenzylammonium lead iodide [$(R\text{-MBA})_2PbI_4$ and $(S\text{-MBA})_2PbI_4$] [5,18,19], were synthesized according to the methodologies outlined in Ref. [19]. The synthesis commenced with the reaction of either *R*- or *S*-MBA (255 µL, 2 mM) with PbO (223.2 mg, 1 mM) in a mixture of 57% HI (5 mL) and H_3PO_2 (1 mL) at 150 °C for 30 min. Following the reaction, the product was allowed to cool to room temperature over a period of 100 h to facilitate the formation of single crystals. These single crystals were then dissolved in *N*,*N*-dimethylformamide (DMF) to achieve a concentration of 10 wt % and subsequently spin-coated onto Si/SiO_2 substrates at 6000 rpm for 30 s to form a thin film. After deposition, the film was annealed at 100 °C for 10 min. Prior to spin coating, the Si/SiO_2 substrate were subjected to cleaning in a UV-ozone cleaner (ASM401N, Asumigiken Ltd.) for 5 min to ensure an uncontaminated surface for film growth.

*Contact author: shoya.sakamoto@issp.u-tokyo.ac.jp
†Contact author: miwa@issp.u-tokyo.ac.jp

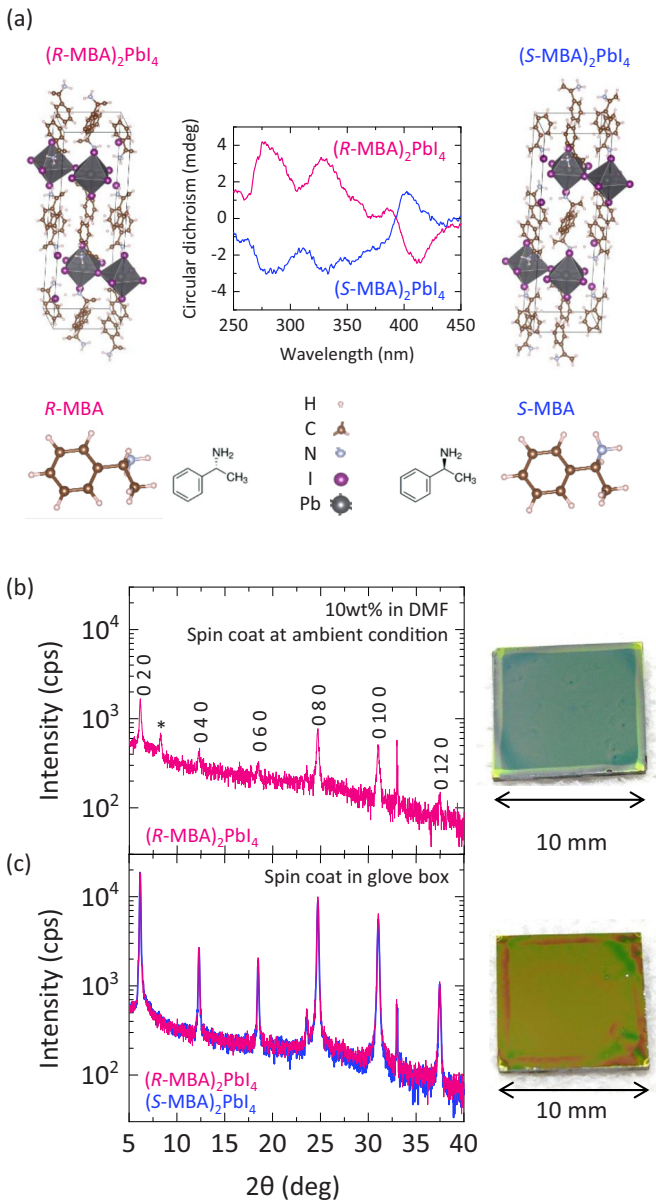

FIG. 1. (a) Schematic of the molecular structures of (*R*)-(+)-α-methylbenzylammonium lead iodide and (*S*)-(−)-α-methylbenzylammonium lead iodide [(*R* -MBA)$_2$PbI$_4$ and (*S* -MBA)$_2$PbI$_4$] [19]. Circular dichroism spectra for (*R* -MBA)$_2$PbI$_4$ and (*S* -MBA)$_2$PbI$_4$ thin films prepared on the quartz substrate. (b) X-ray diffraction results of (*R*-MBA)$_2$PbI$_4$ thin film spin coated at ambient condition. (c) X-ray diffraction results of (*R*-MBA)$_2$PbI$_4$ and (*S*-MBA)$_2$PbI$_4$ thin film spin coated in a nitrogen-filled glove box.

Figure 1(a) shows the transmission circular dichroism (CD) spectra for (*R* -MBA)$_2$PbI$_4$ and (*S* -MBA)$_2$PbI$_4$ thin films prepared on quartz substrate, obtained using a CD spectrometer (J-1500, JASCO, Japan). The CD spectra exhibit distinct derivative features, with (*R* -MBA)$_2$PbI$_4$ shown in red and the (*S* -MBA)$_2$PbI$_4$ in blue. Several peaks with opposite signs, indicative of molecular chirality, are clearly visible in the spectra. Figures 1(b) and 1(c) show the x-ray diffraction results of chiral perovskite films fabricated using the method described above. Figure 1(b) illustrates the results for films prepared under ambient conditions, while Fig. 1(c) details those for films spin-coated in a nitrogen-filled glove box. In both cases, the diffraction peaks marked in black (such as 020, 040, etc.) confirms the presence of a well-oriented 2D structure, characteristic of the *Pnma* space group [19]. Notably, films fabricated in ambient conditions show an additional impurity peak (∼8.3 °, marked with an asterisk). Conversely, films prepared in a glove box exhibit nearly perfect 2D crystallinity, devoid of such an impurity peak. These findings underscore the critical role of glove box conditions in achieving high-quality 2D chiral perovskite thin films. The spin pumping experiments, which are elaborated upon subsequently, utilized the films depicted in Fig. 1(c).

The spin pumping experiments involved multilayer films, comprising a 5-nm-thick $Ni_{81}Fe_{19}$ layer deposited on the approximately 60-nm-thick 2D chiral perovskite films, as depicted in Fig. 2(a). The NiFe layer was deposited using electron beam evaporation under ultrahigh vacuum. To preserve the NiFe surface integrity, a 5-nm layer of MgO followed by a 20-nm layer of SiO_2 was subsequently deposited, the former by electron bean evaporation and the latter via sputtering. TRMOKE measurements were conducted employing a femtosecond pulse laser at a wavelength of 515 nm (carbide CB5-SP and HIRO, light conversion), adhering to the standard pump probe technique [20,21] as shown in Fig. 2(a). The pump light had a power of 44 mW and a spot diameter of 600 μm, while the probe light had a power of 8 mW and a spot diameter of 150 μm. The pulse width of the laser light was 190 fs, with a repetition frequency of 50 kHz.

III. RESULTS

Figure 2(b) shows the magnetization curves for NiFe films deposited on 2D chiral perovskites, (*R*-MBA)$_2$PbI$_4$ and (*S*-MBA)$_2$PbI$_4$, as measured by the magneto-optical Kerr effect with perpendicular magnetic field ($\theta_B = 0°$). NiFe typically exhibits in-plane magnetization, and the observed saturation of magnetization in the perpendicular direction around 0.5 T demonstrates the similar magnetic properties of NiFe across both types of chiral perovskites films, suggesting comparable film quality between (*R*-MBA)$_2$PbI$_4$/NiFe and (*R*-MBA)$_2$PbI$_4$/NiFe systems. In Fig. 2(c), the TRMOKE measurement results for the (*R*-MBA)$_2$PbI$_4$/NiFe are presented. These measurements, conducted under a constant magnetic field of ±2 T angled 25° from the film normal, reveal a pronounced initial drop in the Kerr rotation angle at zero delay time, followed by distinct oscillations as the Kerr rotation magnitude gradually recovers. This immediate decrease in Kerr rotation angle is attributed to ultrafast demagnetization [22,23] in the NiFe layer induced by the pump light, with subsequent oscillations reflecting the perpendicular component of NiFe's magnetization oscillating at the ferromagnetic resonant frequency, i.e., free induction decay. Figure 2(d) shows similar TRMOKE measurement outcomes for (*S*-MBA)$_2$PbI$_4$/NiFe, almost mirroring the results observed for (*R*-MBA)$_2$PbI$_4$/NiFe. The analysis of these oscillations was conducted by fitting the data in the delay-time (t) range 75–500 ps using the equation $A\exp(-t/\tau)\cos(2\pi ft + \varphi) +$

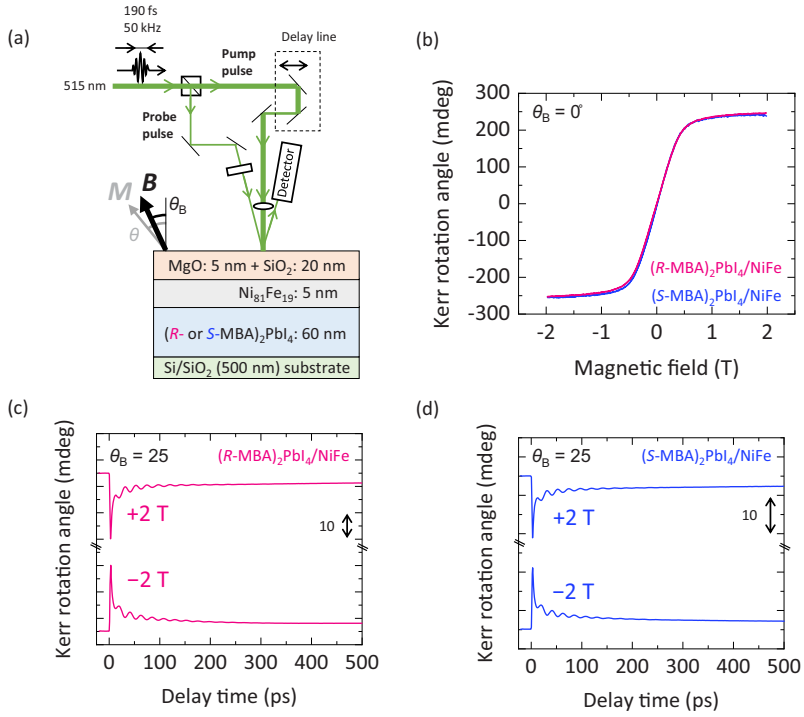

FIG. 2. (a) Schematic of the sample structure and measurement setup. (b) Magnetization hysteresis curve of NiFe. (c), (d) Results of TRMOKE measurements of NiFe grown on $(R\text{-MBA})_2PbI_4$ and $(S\text{-MBA})_2PbI_4$.

$a_0 + a_1 t + a_2 t^2 + a_3 t^3 + a_4 t^4 + a_5 t^5$, where f represents the ferromagnetic resonant frequency and τ the relaxation time.

Figure 3 shows the analysis of the free induction decay observed in the TRMOKE measurements. Specifically, Figs. 3(a) and 3(b) detail the dependence of the resonant frequency on the external magnetic field for the $(R\text{-MBA})_2PbI_4$/NiFe and $(S\text{-MBA})_2PbI_4$/NiFe systems, respectively. The relationship between the magnetic field (B) and the resonant frequency (f) was analyzed using the following Eq. (1) [20]:

$$f = \frac{\gamma}{2\pi}\sqrt{B_1 B_2}$$
$$B_1 = B\cos(\theta - \theta_B) + B_k^{\text{eff}}\cos^2\theta$$
$$B_2 = B\cos(\theta - \theta_B) + B_k^{\text{eff}}\cos 2\theta$$
$$B\sin(\theta_B - \theta) - \frac{1}{2}B_k^{\text{eff}}\sin 2\theta = 0, \quad (1)$$

where $\gamma/2\pi$ (28.0 GHz/T), θ, and $\theta_B(=25^\circ)$ represent gyromagnetic ratio, magnetization angle from film normal, and magnetic field angle [Fig. 2(a)], respectively. Using Eq. (1), the magnetic anisotropy field (B_k^{eff}) of the NiFe layer was estimated based on the results depicted in Figs. 3(a) and 3(b). For the NiFe deposited on $(R\text{-MBA})_2PbI_4$, as shown in Fig. 3(a), θ and B_k^{eff} were determined to be 33° and −0.61 T, respectively. Similarly, for NiFe on $(S\text{-MBA})_2PbI_4$, presented in Fig. 3(b), θ and B_k^{eff} were calculated to be 32° and −0.55 T.

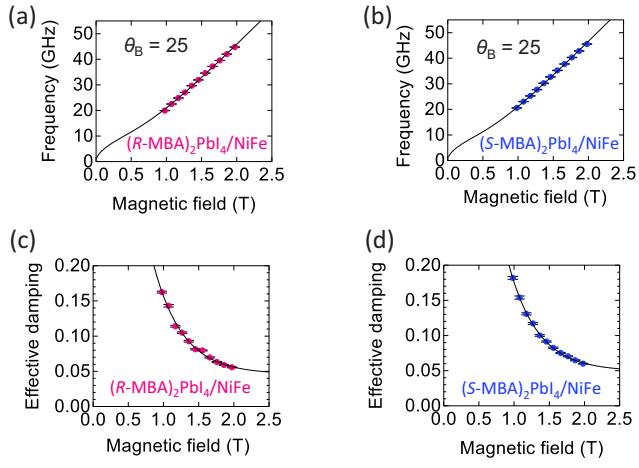

FIG. 3. (a), (b) Resonant frequency and (c), (d) effective damping constant of NiFe grown on $(R\text{-MBA})_2PbI_4$ and $(S\text{-MBA})_2PbI_4$.

To estimate the effective damping constant of the NiFe layer (α_{eff}), Eq. (2) is employed:

$$\frac{1}{\tau} = \frac{1}{2}\alpha_{\text{eff}}\gamma(B_1 + B_2). \quad (2)$$

The analysis of the effective damping for $(R\text{-MBA})_2PbI_4$/NiFe and $(S\text{-MBA})_2PbI_4$/NiFe, as depicted in Figs. 3(c) and 3(d), reveals a notable trend: the effective damping constant decreases monotonically with increasing external magnetic field. This behavior diverges from the expectation that the intrinsic damping inherent to the ferromagnetic metal would remain largely unaffected by

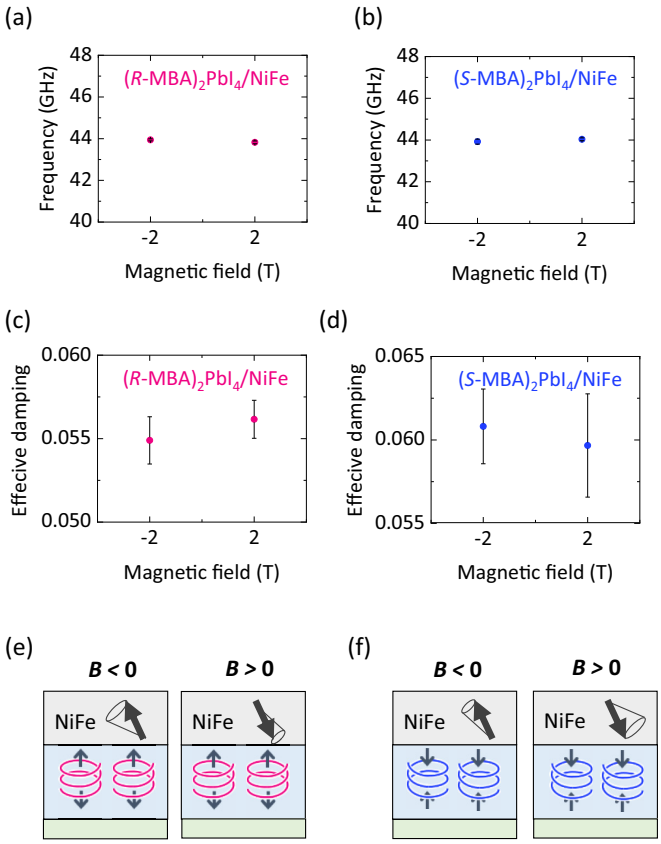

FIG. 4. (a), (b) Comparison of the resonant frequency and (c), (d) the effective damping constant between positive and negative magnetic fields. (e), (f) Schematic drawing of the spin polarization in the chiral perovskites. Black arrows express the direction of spin angular momenta.

variations in the external magnetic field. The observed decrease in the effective damping suggests a substantial influence from extrinsic mechanisms, such as anisotropy dispersion [24] and two-magnon scattering [25], beyond the intrinsic damping contributions. Even at a magnetic field of 2 T, the effective damping continues to decrease monotonically with the magnetic field. By fitting the effective damping to an exponential function of the external magnetic field, we derive the black curves in Figs. 3(c) and 3(d). From these curves, the intrinsic damping constant are extrapolated, yielding values of 0.046 for the system depicted in Fig. 3(c) and 0.049 for that in Fig. 3(d).

The impact of magnetic field direction on the resonant frequency and effective damping constants is shown in Fig. 4. Here, for accurate measurements, the magnetic field was alternated between +2 T and −2 T for a total of 48 measurements (+2 T → −2 T → +2 T…), and the analyzed results are presented in Fig. 4. Error bars represent the standard deviation. As can be seen for (R -MBA)$_2$PbI$_4$/NiFe, the damping constant at +2 T is slightly (∼0.001) higher than at −2 T. Conversely, for (S -MBA)$_2$PbI$_4$/NiFe, the damping constant at +2 T is marginally (∼0.001) lower than at −2 T. Although the variations in the damping constant fall within the error range, the experiment demonstrates that the additional damping of NiFe, induced by the chirality of perovskite layer, is extremely small.

IV. DISCUSSION

It is intriguing to examine the changes in the damping constants of NiFe, particularly from the perspective of CISS in 2D chiral perovskites. We initially consider (i) different spin transparency [26–28] at the interface. Assuming a spin filtering effect at the chiral molecule/metal interface that allows only spins of a specific orientation to pass, based on the observed results of substantial MR effects [5], it is suggested that a spin current cannot enter the chiral molecule in an antiparallel alignment, thus not increasing NiFe damping. Conversely, in a parallel alignment, spin current is injected into the chiral molecule, potentially leading to an increase in NiFe damping. If the significant CISS-induced MR effect reported indeed stems from spin filtering effect, this should manifest as a significant difference in NiFe damping. However, the chirality-induced change in the damping constant observed in this study was negligibly small, as illustrated in Figs. 4(c) and 4(d). In fact, considering the intrinsic damping constant of NiFe (5 nm) on a Si/SiO$_2$ substrate, as determined from separate measurements (not shown), to be 0.005 ± 0.002, the increase in intrinsic damping of NiFe due to spin pumping is estimated at ∼0.04. Consequently, the damping difference of ∼0.001, when considered in the context of spin injection from NiFe to (R -MBA)$_2$PbI$_4$, is likely to represent at most a few percent of the difference of the spin injection. Note that this observation is not consistent with the spin filtering effect deduced from the substantial CISS-induced MR effect [5].

Next, we consider another possibility: (ii) different coupled spin dynamics of ferromagnet and chiral molecules. If chiral molecules exhibit spontaneous spin polarization at the interface [8–13], in a parallel configuration, the spins of the ferromagnet and chiral molecule would perform coherent precession, which should not increase the damping of NiFe. Conversely, in an antiparallel configuration, the induced inhomogeneous spin alignment could potentially increase the damping of NiFe. Although the TRMOKE results in this paper have large errors and do not allow for definitive conclusions about polarity, this scenario is considered the most plausible explanation. Reflecting on previous studies of the (R -MBA)$_2$PbI$_4$/ferromagnet regarding CISS-induced MR effects [5], it was observed that electrical resistance increases when the magnetization (spin angular momentum) of a ferromagnet is directed towards (outwards from) the (R -MBA)$_2$PbI$_4$. Considering spin blockade as the underlying mechanism for the MR effect [29], where electrical resistance increases due to Pauli's exclusion principle when the spin polarization of the chiral molecule and conduction electrons are parallel, the spin angular momentum in (R -MBA)$_2$PbI$_4$ is illustrated as in Fig. 4(e). The orientation of spin angular momentum depicted in Fig. 4(e) aligns with theoretical predictions, assuming that the charger carriers in (R -MBA)$_2$PbI$_4$ are electrons and the spin-orbit interaction is positive. From scenario (ii) described above, the damping constant of NiFe is expected to increase when the spin angular momenta of NiFe and (R -MBA)$_2$PbI$_4$ are antiparallel. Conversely, it would de-

crease when these spin angular momenta are aligned parallel. This consideration regarding the magnitude of the damping constants aligns with the experimental observations at ±2 T, as shown in Fig. 4(c). For the opposite chirality, that is, in the case of (S -MBA)$_2$PbI$_4$/NiFe, the expected direction of spin angular momentum and relative magnitudes of the damping would be reversed, as illustrated in Fig. 4(f).

Several other possibilities should also be considered for the chirality-induced change in the damping constant of NiFe. One is (iii) different spin diffusion length in chiral molecules. When a spin current, polarized in a direction parallel to the electrical current, is injected into chiral molecules, different spin diffusion lengths are expected between R and S enantiomers due to the CISS effect. This effect implies different momentum relaxation times for up-spin and down-spin electrons [13]. If the bulk spin polarization in the chiral molecules is parallel to the spin current, minimal spin relaxation is expected in the chiral molecule, thus suppressing spin diffusion from NiFe to the chiral molecules and resulting in little change to the NiFe's damping constant. Consequently, if the polarity is opposite, significant spin relaxation occurs in the chiral molecules, potentially increasing the NiFe's damping constant. However, this distinction only applies if the thickness of the chiral molecule film is less than the spin diffusion length. In this study, we use a chiral molecule film that is 50 nm thick, with expected spin diffusion length smaller than 50 nm. Therefore, we anticipate minimal effects from this mechanism. Another possibility is (iv) different spin memory loss at the interface. Spin memory loss [30], which is the scattering of spin currents at interfaces due to spin-orbit interactions, is unlikely to differ due to chirality.

Finally, we would like to address the discrepancy between the significant CISS-induced MR effect detected in spin-polarized conductive atomic force microscopy measurements and the modest MR in multilayer device. Previous research using (R -MBA)$_2$PbI$_4$ reported a CISS-induced MR effect of 86%, utilizing the spin-polarized conductive atomic force microscopy. In contrast, with multilayer device approaches, the MR ratio remained below 0.5% [5]. Similar outcomes have been reported with other chiral molecules and ferromagnetic metals, often attributing pinholes in the chiral molecules as obstacles to the injection of spin-polarized electric currents [6]. However, the difference in damping constants noted in this study aligns more closely with the lower values observed in multilayer devices than with the higher values from spin-polarized conductive atomic force microscopy. This measurement, conducted using the spin pumping method without current injection, is unaffected by pinholes that typically complicate current injection experiments. Consequently, the minimal difference in damping constants, indicating a minor CISS, strongly implies that the differences in CISS observed between the spin-polarized conductive atomic force microscopy and multilayer device methods may stem from fundamentally distinct physical mechanisms. Specifically, the absence of significant chirality-induced damping in this study suggests that the origin of the substantial CISS-induced MR using the spin-polarized conductive atomic force microscopy is unlikely to be due to the spin filtering effect.

V. CONCLUSION

In this research, we investigated CISS-related phenomena in the (R - or S -MBA)$_2$PbI$_4$/NiFe system employing the spin pumping method, which notably does not require the injection of electric current. Our experiments revealed a subtle yet observable CISS, manifesting as variation in the NiFe damping constant in relation to the magnetization direction. This observation was made in a charge-current-free environment, specifically chosen to avoid the problem of pinholes commonly encountered in multilayer devices using chiral molecules to measure the CISS-induced MR effect. When comparing the variations in damping constants observed in this study to previously reported MR effects, our results align more closely with the moderate MR noted in a multilayer device rather than the substantial MR detected via spin-polarized conductive atomic force microscopy. Our results suggest that the underlying mechanisms of the MR effects associated with CISS in both conductive atomic force microscopy and multilayer device configurations are not due to the difference in pinholes, but may be fundamentally different. We believe that our findings contribute valuable insights into the understandings of CISS-related phenomena, paving the way for further research in this field.

ACKNOWLEDGMENTS

We thank K. Kondou of RIKEN for discussion. This work was partially supported by JSPS-KAKENHI (Grants No. 22K18320, No. 22H00290, No. 22H04964, and No. 24H02234), JST-ASPIRE (Grant No. JPMJAP2317), Spintronics Research Network of Japan (Spin-RNJ), MEXT Initiative to Establish Next-Generation Novel Integrated Circuit Centers (X-NICS) (Grant No. JPJ011438), and MEXT Promotion of Development of a Joint Usage/Research System Project: Coalition of Universities for Research Excellence Program (CURE) (Grant No. JPMXP1323015482).

[1] B. Göhler, V. Hamelbeck, T. Z. Markus, M. Kettner, G. F. Hanne, Z. Vager, R. Naaman, and H. Zacharias, Spin selectivity in electron transmission through self-assembled monolayers of double-stranded DNA, Science **331**, 894 (2011).

[2] Z. Xie, T. Z. Markus, S. R. Cohen, Z. Vager, R. Gutierrez, and R. Naaman, Spin specific electron conduction through DNA oligomers, Nano Lett. **11**, 4652 (2011).

[3] K. Banerjee-Gshosh, O. Ben Dor, F. Tassinari, E. Capua, S. Yochelis, A. Capua, S.-H. Yang, S. S. P. Parkin, S. Sarkar, L. Kronik, L. T. Baczewski, R. Naaman, and Y. Paltiel, Separation of enantiomers by their enentiospecific interaction with achiral magnetic substrates, Science **360**, 1331 (2018).

[4] R. Naaman, Y. Paltiel, and D. H. Waldeck, Chiral molecules and the electron spin, Nat. Rev. Chem. **3**, 250 (2019).

[5] H. Lu, J. Wang, C. Xiao, X. Pan, X. Chen, R. Brunecky, J. J. Berry, K. Zhu, M. C. Beard, and Z. V. Vardeny, Spin-dependent charge transport through 2D chiral hybrid lead-iodide perovskites, Sci. Adv. **5**, eaay0571 (2019).

[6] C. Kulkarni, A. K. Mondal, T. K. Das, G. Grinbom, F. Tassinari, M. F. J. Mabesoone, E. W. Meijer, and R. Naaman, Highly efficient and tunable filtering of electrons' spin by supramoleuclar chirality of nanofiber-based materials, Adv. Mater. **32**, 1904965 (2020).

[7] S.-H. Yang, R. Naaman, Y. Paltiel, and S. S. P. Parkin, Chiral spintronics, Nat. Rev. Phys. **3**, 328 (2021).

[8] S. Miwa, K. Kondou, S. Sakamoto, A. Nihonyanagi, F. Araoka, Y. Otani, and D. Miyajima, Chirality-induced effective magnetic field in a phthalocyanine molecule, Appl. Phys. Express **13**, 113001 (2020).

[9] N. Sukenik, F. Tassinari, S. Yochelis, O. Millo, L. T. Baczewski, and Y. Paltiel, Correlation between ferromagnetic layer easy axis and the tilt angle of self assembled chiral moleucles, Molecules **25**, 6036 (2020).

[10] N. Goren, S. Yochelis, G. Jung, and Y. Paltiel, Magnetic passivation using chiral molecules, Appl. Phys. Lett. **118**, 172401 (2021).

[11] J. Fransson, Charge redistribution and spin polarization driven by correlation induced electron exchange in chiral molecules, Nano Lett. **21**, 3026 (2021).

[12] K. Kondou, M. Shiga, S. Sakamoto, H. Inuzuka, A. Nihonyanagi, F. Araoka, M. Kobayashi, S. Miwa, D. Miyajima, and Y. Otani, Chirality-induced magnetoresistance due to thermally driven spin polarization, J. Am. Chem. Soc. **144**, 7302 (2022).

[13] K. Kondou, S. Miwa, and D. Miyajima, Spontaneous spin selectivity in chiral molecules at the interface, J. Magn. Magn. Mater. **585**, 171157 (2023).

[14] X. Yang, C. H. van der Wal, and B. J. van Wees, Spin-dependent electron transmission model for chiral molecules in mesoscopic devices, Phys. Rev. B **99**, 024418 (2019).

[15] S. Mizukami, Y. Ando, and T. Miyazaki, Effect of spin diffusion on Gilbert damping for a very thin permalloy layer in Cu/permalloy/Cu/Pt films, Phys. Rev. B **66**, 104413 (2002).

[16] Y. Tserkovnyak and A. Brataas, Enhanced Gilbert damping in thin film ferromagnetc films, Phys. Rev. Lett. **88**, 117601 (2002).

[17] K. Ando, S. Takahashi, J. Ieda, H. Kurebayashi, T. Trypiniotis, C. H. W. Barnes, S. Maekawa, and E. Saitoh, Electrically tunable spin injector free from the impedance mismatch problem, Nat. Mater. **10**, 655 (2011).

[18] J. Ma, C. Fang, C. Chen, L. Jin, J. Wang, S. Wang, J. Tang, and D. Li, Chiral 2D perovskites with a high degree of cirularly polarized photoluminescence, ACS Nano **13**, 3659 (2019).

[19] Y. Dang, X. Liu, Y. Sun, J. Song, W. Hu, and X. Tao, Bulk chiral halide perovskite single crystal for active circular dichroism and circularly polarized luminescence, J. Phys. Chem. Lett. **11**, 1689 (2020).

[20] S. Iihama, S. Mizukami, H. Naganuma, M. Oogane, Y. Ando, and T. Miyazaki, Gilbert damping constants of Ta/CoFeB/MgO(Ta) thin films measured by optical detection of precessional magnetization dynsmics, Phys. Rev. B **89**, 174416 (2014).

[21] S. Miwa, S. Iihama, T. Nomoto, T. Tomita, T. Higo, M. Ikhlas, S. Sakamoto, Y. Otani, S. Mizukami, R. Arita, and S. Nakatsuji, Giant effective damping of octupole oscillation in an antiferromagnetic Weyl semimetal, Small Sci. **1**, 2000062 (2021).

[22] E. Beaurepaire, J.-C. Merle, A. Daunois, and J.-Y. Bigot, Ultrafast spin dynamics in ferromagnetic nickel, Phys. Rev. Lett. **76**, 4250 (1996).

[23] A. Kirilyuk, A. V. Kimel, and T. Rasing, Ultrafast optical manipulation of magnetic order, Rev. Mod. Phys. **82**, 2731 (2010).

[24] G. Malinowski, K. C. Kuiper, R. Lavrijsen, H. J. M. Swagten, and B. Koopmans, Magnetization dynamics and Gilbert damping in ultrathin $Co_{48}Fe_{32}B_{20}$ films with out-of-plane anisotropy, Appl. Phys. Lett. **94**, 102501 (2009).

[25] J. Lindner, I. Barsukov, C. Raeder, C. Hassel, O. Posth, R. Meckenstock, P. Landeros, and D. L. Mills, Two-magnon damping in thin films in case of canted magnetization: Theory versus experiment, Phys. Rev. B **80**, 224421 (2009).

[26] A. Brataas, Yu. V. Nazarov, and G. E. W. Bauer, Finite-element theory of transport in ferromagnet-normal metal systems, Phys. Rev. Lett. **84**, 2481 (2000).

[27] Y.-T. Chen, S. Takahashi, H. Nakayama, M. Althammer, S. T. B. Goennenwein, E. Saitoh, and G. E. W. Bauer, Theory of spin Hall magnetoresistance, Phys. Rev. B **87**, 144411 (2013).

[28] W. Zhang, W. Han, X. Jiang, S.-H. Yang, and S. S. P. Parkin, Role of transparency of platinum–ferromagnet interfaces in determining the intrinsic magnitude of the spin Hall effect, Nat. Phys. **11**, 496 (2015).

[29] R. Naaman, Y. Paltiel, and D. H. Waldeck, Chiral molecules and the spin selectivity effect, J. Phys Chem. Lett. **11**, 3660 (2020).

[30] J.-C. Rojas-Sánchez, N. Reyren, P. Laczkowski, W. Savero, J.-P. Attané, C. Deranlot, M. Jamet, J.-M. George, L. Vila, and H. Jaffrès, Spin pumping and inverse spin Hall effect in platinum: The essential role of spin-memory loss at metallic interfaces, Phys. Rev. Lett. **112**, 106602 (2014).